Anomalously weak solar convection

Shravan M. Hanasoge[a,b,1], Thomas L. Duvall, Jr.[c], and Katepalli R. Sreenivasan[d]

[a]Department of Geosciences, Princeton University, NJ 08544; [b]Max-Planck-Institut für Sonnensystemforschung, 37191 Katlenburg-Lindau, Germany; [c]Solar Physics Laboratory, National Aeronautics and Space Administration (NASA)/Goddard Space Flight Center, MD 20771; and [d]Courant Institute of Mathematical Sciences, New York University, NY 10012

Contributed by Katepalli R. Sreenivasan, May 3, 2012 (sent for review December 30, 2011)

Convection in the solar interior is thought to comprise structures on a spectrum of scales. This conclusion emerges from phenomenological studies and numerical simulations, though neither covers the proper range of dynamical parameters of solar convection. Here, we analyze observations of the wavefield in the solar photosphere using techniques of time-distance helioseismology to image flows in the solar interior. We downsample and synthesize 900 billion wavefield observations to produce 3 billion cross-correlations, which we average and fit, measuring 5 million wave travel times. Using these travel times, we deduce the underlying flow systems and study their statistics to bound convective velocity magnitudes in the solar interior, as a function of depth and spherical-harmonic degree ℓ. Within the wavenumber band $\ell < 60$, convective velocities are 20–100 times weaker than current theoretical estimates. This constraint suggests the prevalence of a different paradigm of turbulence from that predicted by existing models, prompting the question: what mechanism transports the heat flux of a solar luminosity outwards? Advection is dominated by Coriolis forces for wavenumbers $\ell < 60$, with Rossby numbers smaller than approximately 10^{-2} at $r/R_\odot = 0.96$, suggesting that the Sun may be a much faster rotator than previously thought, and that large-scale convection may be quasi-geostrophic. The fact that isorotation contours in the Sun are not coaligned with the axis of rotation suggests the presence of a latitudinal entropy gradient.

imaging | thermal wind balance | Reynolds stresses | inverse problem

The thin photosphere of the Sun, where thermal transport is dominated by free-streaming radiation, shows a spectrum in which granulation and supergranulation are most prominent. Observed properties of granules, such as spatial scales, radiative intensity, and photospheric spectral-line formation are successfully reproduced by numerical simulations (1, 2). In contrast, convection in the interior is not directly observable and likely governed by aspects more difficult to model, such as the integrity of descending plumes to diffusion and various instabilities (3). Further, solar convection is governed by extreme parameters (4) (Prandtl number approximately 10^{-6}–10^{-4}, Rayleigh number approximately 10^{19}–10^{24}, and Reynolds number approximately 10^{12}–10^{16}), which make fully resolved three-dimensional direct numerical simulations impossible for the foreseeable future. It is likewise difficult to reproduce them in laboratory experiments.

Turning to phenomenology, mixing-length theory (MLT) is predicated on the assumption that parcels of fluid of a specified spatial and velocity scale transport heat over one length scale (termed the *mixing length*) and are then mixed in the new environment. While this picture is simplistic (5), it has been successful in predicting aspects of solar structure as well as the dominant scale and magnitude of observed surface velocities. MLT posits a spatial convective scale that increases with depth (while velocities reduce) and coherent large scales of convection, termed *giant cells*. Simulations of anelastic global convection (6, 7, 8, 9), more sophisticated than MLT, support the classical picture of a turbulent cascade. The anelastic spherical harmonic (ASH) simulations (6) solve the nonlinear compressible Navier-Stokes equations in the anelastic limit; i.e., where acoustic waves, which oscillate at very different time scales, are filtered out. Considerable effort has been spent in attempting surface (10) and interior detection (11, 12) of giant cells, but evidence supporting their existence has remained inconclusive.

Results

Here, we image the solar interior using time-distance helioseismology (11–13). Raw data in this analysis are line-of-sight photospheric Doppler velocities measured by the Helioseismic and Magnetic Imager (14) onboard the Solar Dynamics Observatory. Two-point correlations from temporal segments of length T of the observed Doppler wavefield velocities are formed and spatially averaged according to a deep-focusing geometry (15) (Figs. 1 and 2). We base the choice of T on estimates of convective coherence time scales (6, 16, 17). These correlations are then fitted to a reference Gabor wavelet function (18) to obtain travel-time shifts $\delta\tau(\theta, \phi, T)$, where (θ, ϕ) are colatitude and longitude on the observed solar disk. By construction, these time shifts are sensitive to different components of 3D vector flows; i.e., longitudinal, latitudinal, or radial, at specific depths of the solar interior ($r/R_\odot = 0.92$, 0.96) and consequently, we denote individual flow components (longitudinal or latitudinal) by scalars. Each point (θ, ϕ) on the travel-time map is constructed by correlating 600 pairs of points on opposing quadrants. A sample travel-time map is shown in Fig. 3.

Waves are stochastically excited in the Sun, because of which the above correlation and travel-time measurements include components of incoherent wave noise, whose variance (19) diminishes as T^{-1}. The variance of time shifts induced by convective structures that retain their coherence over time scale T does *not* diminish as T^{-1}, allowing us to distinguish them from noise. We may therefore describe the total travel-time variance $\sigma^2(T) \equiv \sum_{\theta,\phi}\langle\delta\tau^2(\theta, \phi, T)\rangle$ as the sum of variances of signal S^2 and noise N^2/T, assuming that S and N are statistically independent. Angled brackets denote ensemble averaging over measurements of $\delta\tau(\theta, \phi, T)$ from many independent segments of temporal length T. Given a coherence time $T_{\rm coh}$, we fit $\sigma^2(T) = S^2 + N^2/T$ over $T < T_{\rm coh}$ to obtain the integral upper limit S. The fraction of the observed travel-time variance that cannot be modeled as uncorrelated noise is therefore $S^2/\sigma^2(T_{\rm coh})$. For averaging lengths $T_{\rm coh}$ (=24 and 96 h) considered here, we find this signal to be small; i.e., $S^2 \ll N^2/T_{\rm coh}$, which leads us to conclude that large-scale convective flows are weak in magnitude. Further, because surface supergranulation contributes to S, our estimates form an upper bound on ordered convective motions.

Spatial scales on spherical surfaces are well characterized in spherical harmonic space:

$$\delta\tau_{\ell m}(T) = \int_0^\pi \sin\theta\, d\theta \int_0^{2\pi} d\phi\, \delta\tau(\theta, \phi, T) Y^*_{\ell m}(\theta, \phi), \qquad [1]$$

Author contributions: S.M.H. and T.L.D. designed research; K.R.S., S.M.H., and T.L.D. performed research; S.M.H. and T.L.D. analyzed data; and S.M.H., T.L.D., and K.R.S. wrote the paper.

The authors declare no conflict of interest.

See Commentary on page 11896.

[1]To whom correspondence should be addressed. E-mail: krs3@nyu.edu.

This article contains supporting information online at www.pnas.org/lookup/suppl/doi:10.1073/pnas.1206570109/-/DCSupplemental.

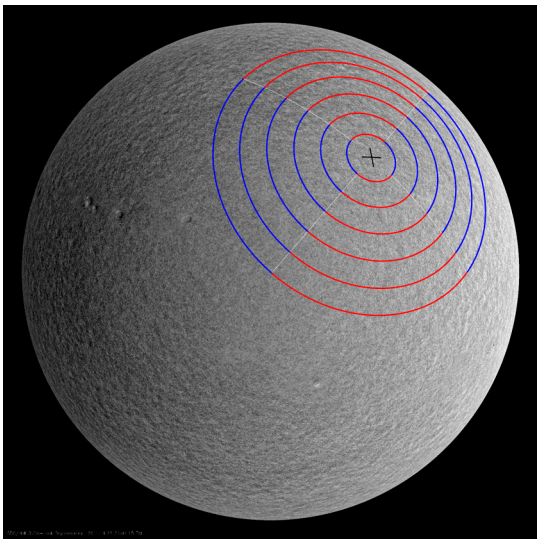

Fig. 1. Line-of-sight Doppler velocities are measured every 45 s at 4, 096 × 4, 096 pixels on the solar photosphere by the Helioseismic and Magnetic Imager (background image). We cross correlate wavefield records of temporal length T at points on opposing quadrants (blue with blue or red with red). These "blue" and "red" correlations are separately averaged, respectively sensitive to longitudinal and latitudinal flow at $(\theta, \phi; r/R_\odot = 0.96)$, where (θ, ϕ) is the central point marked by a cross (see Fig. 2 for further illustration). The longitudinal measurement is sensitive to flows in that direction while the latitudinal measurement to flows along latitude. We create a travel-time maps $\delta\tau(\theta, \phi, T)$ by making this measurement about various central points (θ, ϕ) on the surface. Each travel time is obtained upon correlating the wavefield between 600 pairs of points distributed in azimuth.

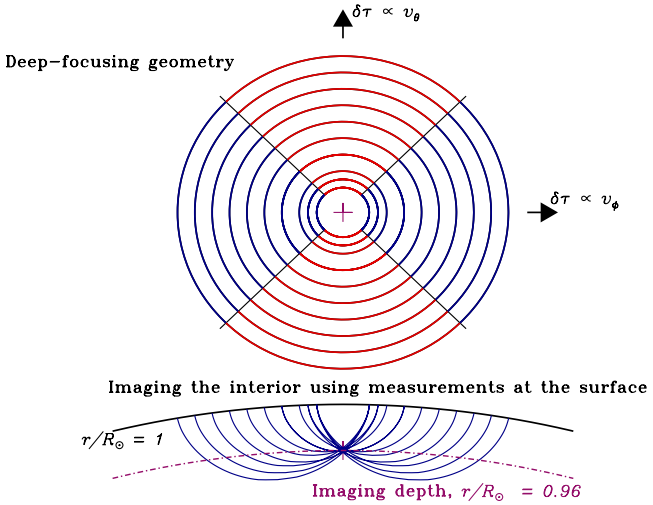

Fig. 2. The cross-correlation measurement geometry (upper box; arrowheads—horizontal: longitude, and vertical: latitude) used to image the layer $r/R_\odot = 0.96$ (dot-dashed line). Doppler velocities of temporal length T measured at the solar surface are cross correlated between point pairs at opposite ends of annular discs (colored red and blue); e.g., points on the innermost blue sector on the left are correlated with diagonally opposite points on the outermost blue sector on the right. Six-hundred correlations are prepared and averaged for each travel-time measurement. Travel times of waves that propagate along paths in the direction of the horizontal and vertical arrows are primarily sensitive to longitudinal and latitudinal flows, v_ϕ and v_θ, respectively. The focus point of these waves is at $r/R_\odot = 0.96$ (lower box) and the measured travel-time shift $\delta\tau(\theta, \phi, T)$ is linearly related to the flow component $v(r/R_\odot = 0.96, \theta, \phi)$ with a contribution from the incoherent wave noise. We are thus able to *map* the flow field at specific depths $v(r, \theta, \phi)$ through appropriate measurements of $\delta\tau(\theta, \phi, T)$. For the inversions here, we create travel-time maps of size 128 × 128 (see Fig. 3). For reference, we note that the base of the convection zone is located at $r/R_\odot = 0.71$ and the near-surface shear layer extends from $r/R_\odot = 0.9$ upwards.

where $Y_{\ell m}$ are spherical harmonics, (ℓ, m) are spherical harmonic degree, and order, respectively, and $\delta\tau_{\ell m}(T)$ are spherical harmonic coefficients. Here, we specifically define the term "scale" to denote $2\pi R_\odot/\sqrt{\ell(\ell+1)}$, which implies that small scales correspond to large ℓ and vice versa. Note that a spatial ensemble of small convective structures such as a granules or intergranular lanes (e.g., as observed on the solar photosphere) can lead to a broad power spectrum that has both small scales and large scales. The power spectrum of an ensemble of small structures, such as granulation patterns seen at the photosphere, leads to a broad distribution in ℓ, which we term here as *scales*. Travel-time shifts $\delta\mathcal{S}_{\ell m}$, induced by a convective flow component $v_{\ell m}(r)$, are given in the single-scattering limit by $\delta\mathcal{S}_{\ell m} = \int_\odot r^2\, dr\, \mathcal{K}_\ell(r) v_{\ell m}(r)$, where $\mathcal{K}_\ell$ is the sensitivity of the measurement to that flow component. The variance of flow-induced time shifts at every scale is bounded by the variance of the signal in observed travel times; i.e., $\langle \delta\mathcal{S}^2_{\ell m}\rangle \leq S^2/\sigma^2(T_{\rm coh})\langle \delta\tau^2_{\ell m}(T_{\rm coh})\rangle$. To complete the analysis, we derive sensitivity kernels $\mathcal{K}_\ell(r)$ that allow us to deduce flow components in the interior, given the associated travel-time shifts (i.e., the *inverse* problem).

The time-distance deep-focusing measurement (15) is calibrated by linearly simulating waves propagating through spatially small flow perturbations, implanted at 500 randomly distributed (known) locations, on a spherical shell at a given interior depth (Fig. 4). This delta-populated flow system contains a full spectrum; i.e., its power extends from small to large spherical harmonic degrees. The simulated data are then filtered both spatially and temporally in order to isolate waves that propagate to the specific depth of interest (termed phase-speed filtering). Travel times of these waves are then measured for focus depths the same as the depths of the features, and subsequently corrected for stochastic excitation noise (22). Note that these corrections may only be applied to simulated data—this is because we have full knowledge of the realization of sources that we put in. Longitudinal and radial flow perturbations are analyzed through separate simulations, giving us access to the full vector sensitivity of this measurement to flows. Travel-time maps from the simulations appear as a low-resolution version of the input perturbation map because of diffraction associated with finite wavelengths of acoustic waves

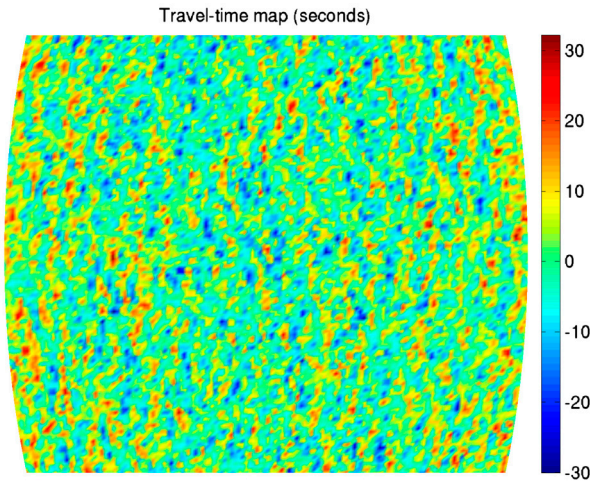

Fig. 3. A travel-time map consisting 16,384 travel-time measurements, spanning a 60° × 60° region (at a resolution of 0.46875 ° per pixel) around the solar disk center, obtained by analyzing one day's worth of data taken by the Helioseismic and Magnetic Imager instrument (14) onboard the Solar Dynamics Observatory satellite. 3.2 billion wavefield measurements were analyzed to generate 10 million correlations, which were averaged and fitted to generate this travel-time map. This geometry and these particular wave times are so chosen as to be sensitive to flow systems in the solar interior. The spectrum of these travel times shows no interesting or anomalous peaks that meet the detection criteria (described subsequently).

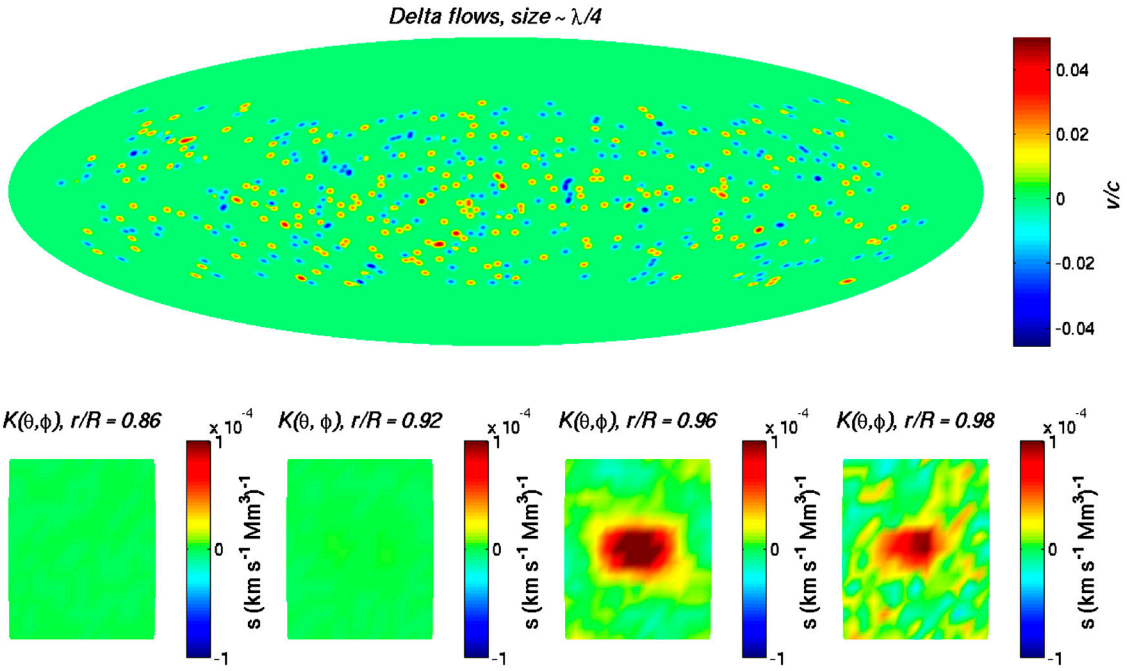

Fig. 4. Because wavelengths of helioseismic waves may be comparable to or larger than convective features through which they propagate, the ray approximation is inaccurate and finite-wavelength effects must be accounted for when modeling wave propagation in the Sun (20). In order to derive the 3D finite-frequency sensitivity function (kernel) associated with a travel-time measurement (21), we simulate waves propagating through a randomly scattered set of 500 east-west-flow 'delta' functions, each of which is assigned a random sign so as not to induce a net flow signal (22) (upper box). We place these flow deltas in a latitudinal band of extent 120° centered about the equator, because the quality of observational data degrades outside of this region. We perform six simulations, with these deltas placed at a different depth in each instance, so as to sample the kernel at these radii. The bottom four boxes show slices at various radii of the sensitivity function for the measurement which attempts to resolve flows at $r/R_\odot = 0.96$. Measurement sensitivity is seen to peak at the focus depth, a desirable quality, but contains near-surface lobes as well. Note that the volume integral of flows in the solar interior with this kernel function gives rise to the associated travel-time shift, which explains the units.

excited in the Sun and in the simulations. The connection between the two maps is primarily a function of spherical-harmonic degree ℓ. To quantify the connection, both images are transformed and a linear regression is performed between coefficients of the two transforms at each ℓ separately (see *SI Appendix* for details). The slope of this linear regression is the calibration factor for degree ℓ.

We apply similar analyses to 27 d of data (one solar rotation) taken by the Helioseismic and Magnetic Imager from June-July 2010. These images are tracked at the Carrington rotation rate, interpolated onto a fine latitude-longitude grid, smoothed with a Gaussian, and resampled at the same resolution as the simulations (0.46875 deg /pixel). The data are transformed to spherical harmonic space and temporal Fourier domain, phase-speed filtered (as described earlier) and transformed back to the real domain. Cross-correlations and travel times are computed with the same programs as used on the simulations. Strips of 13 ° of longitude and the full latitude range are extracted from each of the 27 d results and combined into a synoptic map covering a solar rotation. The coefficients from the spherical harmonic transform of this map are converted, at each degree ℓ, by the calibration slope mentioned above, and a resultant flow spectrum is derived, as shown in Fig. 5. These form observational upper bounds on the magnitude of turbulent flows in the convection zone at the scales to which the measurements are sensitive.

It is seen that constraints in Fig. 5 become poorer with greater imaging depth. This trend may be attributed to diffraction, which limits seismic spatial resolution to approximately a wavelength. In turn, the acoustic wavelength, proportional to sound speed, increases with depth. Because density also grows rapidly with depth, the velocity required to transport the heat flux of a solar luminosity decreases, a prediction echoed by all theories of solar convection. Thus we may reasonably conclude that the $r/R_\odot = 0.96$ curve is also the upper bound for convective velocities at deeper layers in the convective zone (although the constraint at $r/R_\odot = 0.92$ curve is weaker due to a coarser diffraction limit). Less restrictive constraints obtained at depths $r/R_\odot = 0.79, 0.86$ (whose quality is made worse by the poor signal-to-noise ratio) are not displayed here.

Discussion

Convective Transport. The spectral distribution of power due to an ensemble of convective structures, of spatial sizes small or large or both, will be broad. For example, it has been argued (10) that photospheric convection comprises only granules and supergranules, and that the power spectrum of an ensemble of these structures would extend from the lowest to highest ℓ. In other words, if granulation-related flow velocities were to be altered, the *entire* power spectrum would be affected. Thus the large scales which we image here (i.e., power for low ℓ), contain contributions from small and large structures alike, and represent, albeit in a complicated and incomplete manner, gross features of the transport mechanism.

Our constraints show that for wavenumbers $\ell < 60$, flow velocities associated with solar convection ($r/R_\odot = 0.96$) are substantially smaller than current predictions. Alternately one may interpret the constraints as a statement that the temporal coherence of convective structures is substantially shorter than predicted by current theories. Analysis of numerical simulations (6) of solar convection shows that a dominant fraction (approximately 80%) of the heat transport is effected by the small scales, However, our observations show that the simulated velocities are substantially overestimated in the wavenumber band $\ell < 60$, placing in question (based on the preceding argument) the entire predicted spectrum of convective flows and the conclusions derived thereof. We further state that we lack definitive knowledge on the energy-carrying scales in the convection zone. We may thus

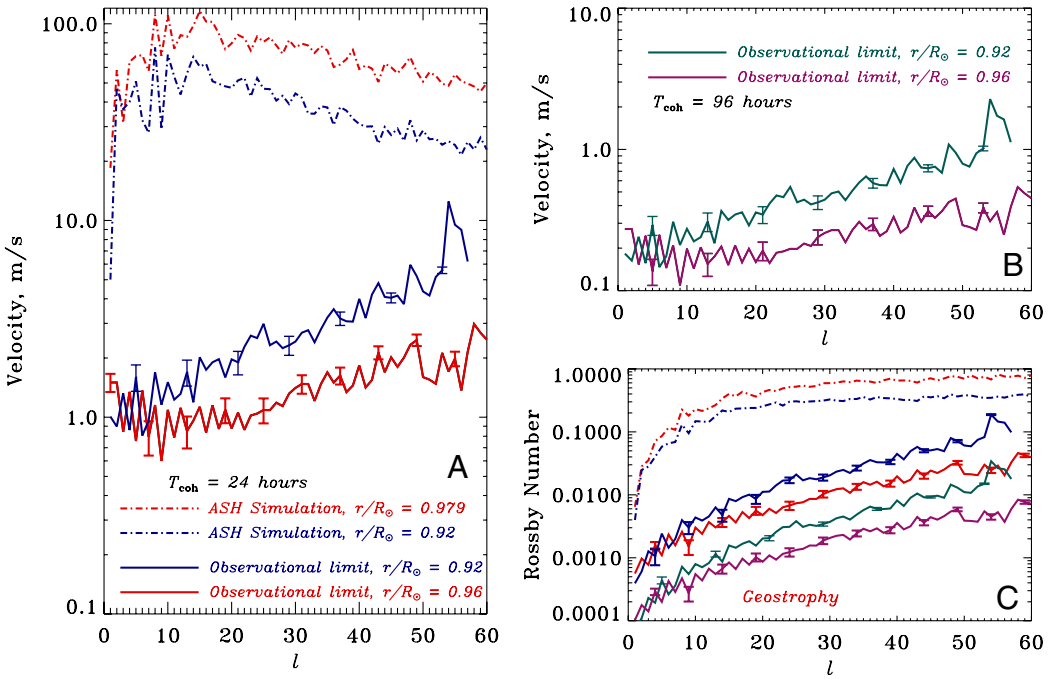

Fig. 5. Observational bounds on flow magnitudes and the associated Rossby numbers. Boxes (*A*, *B*): solid curves with 1-σ error bars (standard deviations) show observational constraints on lateral flows averaged over *m* at radial depths, $r/R_\odot = 0.92, 0.96$; dot-dash lines are spectra from ASH convection simulations (6). Colors differentiate between the focus depth of the measurement and coherence times. At a depth of $r/R_\odot = 0.96$, simulations of convection (6) show a coherence time of $T_{coh} = 24$ hours (*A*) while MLT (16) gives $T_{coh} = 96$ hours (*B*), the latter obtained by dividing the mixing length by the predicted velocity. Both MLT and simulations (23, 24) indicate a convective depth coherence over 1.8 pressure scale heights, an input to our inversion. At $r/R_\odot = 0.96$, MLT predicts a 60 ms^{-1}, $\ell = 61$ convective flow and for $r/R_\odot = 0.92$, an $\ell = 33$, 45 ms^{-1} flow [upon applying continuity considerations (23)]. (*C*) shows upper bounds on Rossby number, $Ro = U/(2\Omega L)$, $L = 2\pi r/\sqrt{\ell(\ell+1)}$, $r = 0.92$, 0.96 $R_\odot$. Interior convection appears to be strongly geostrophically balanced (i.e., rotationally dominated) on these scales. By construction, these measurements are sensitive to lateral flows i.e., longitudinal and latitudinal at these specific depths ($r/R_\odot = 0.92$, 0.96) and consequently, we denote these flow components (longitudinal or latitudinal) by scalars.

ask: how would this paradigm of turbulence affect extant theories of dynamo action?

For example, consider the scenario discussed by Spruit in ref. 25, who envisaged very weak upflows, which, seeded at the base of the convection zone, grow to ever larger scales due to the decreasing density as they buoyantly rise. These flows are in mass balance with cool intergranular plumes which, formed at the photosphere, are squeezed ever more so as they plunge into the interior. Such a mechanism presupposes that these descending plumes fall nearly ballistically through the convection zone, almost as if a cold sleet, amid warm upwardly diffusing plasma. In this schema, individual structures associated with the transport process would elude detection because the upflows would be too weak and the downflows of too small a structural size. When viewed in terms of spherical harmonics, the associated velocities at large scales (i.e., low ℓ), which contain contributions from both upflows and descending plumes, would also be small. Whatever mechanism may prevail, the stability of descending plumes at high Rayleigh and Reynolds numbers and very low Prandtl number is likely to play a central role (3, 25).

Differential Rotation and Meridional Circulation. Differential rotation, a large-scale feature ($\ell \sim 2$), is one individual global flow system and easily detected in our travel-time maps. Differential rotation is the only feature we "detect" within this wavenumber band. In other words, upon subtracting this $\ell = 2$ feature from the travel-time maps, the variance of the remnant falls roughly as T^{-1}, where T is the temporal averaging length, suggesting the nonexistence of other structures at these scales. Consequently, we may assert that we do not see evidence for a "classical" inverse cascade that results in the production of a smooth distribution of scales.

Current models of solar dynamo action posit that differential rotation drives the process of converting poloidal to toroidal flux. This process would result in a continuous loss of energy from the differentially rotating convective envelope and Reynolds' stresses have long been thought of as a means to replenish and sustain the angular velocity gradient. The low Rossby numbers in our observations indicate that turbulence is geostrophically arranged over wavenumbers $\ell < 60$ at the depth $r/R_\odot = 0.96$, further implying very weak Reynolds stresses. Because flow velocities are likely to become weaker with depth in the convection zone, the Rossby numbers will decrease correspondingly. At wavenumbers of $\ell \sim 2$, the thermal wind balance equation describing geostrophic turbulence likely holds extremely well within most of the convection zone:

$$\Omega_0 \frac{\partial \Omega}{\partial z} = \frac{C}{r^2 \sin\theta} \frac{\partial S}{\partial \theta}, \qquad [2]$$

where Ω_0 is the mean solar rotation rate, Ω is the differential rotation, z is the axis of rotation, θ is the latitude, C is a constant, S is the azimuthally and temporally averaged entropy gradient. Differential rotation around $\ell \sim 2$ is helioseismically well constrained; i.e., the left side of Eq. **2** is accurately known (e.g., ref. 26). The isorotation contours are not coaligned with the axis of rotation, yielding a nonzero left side of Eq. **2**. Taylor-Proudman balance is broken and we may reasonably infer that the Sun does indeed possess a latitudinal entropy gradient, of a suitable form so as to sustain solar differential rotation (see e.g., refs. 27, 28).

The inferred weakness of Reynolds stresses poses a problem to theories of meridional circulation, which rely on the former to effect angular momentum transport in order to sustain the latter. Very weak turbulent stresses would imply a correspondingly weak meridional circulation (e.g., ref. 29).

ACKNOWLEDGMENTS. All computing was performed on NASA Ames supercomputers: Schirra and Pleiades. S.M.H. acknowledges support from NASA Grant NNX11AB63G and thanks Courant Institute, NYU for hosting him as a visitor. Many thanks to Tim Sandstrom of the NASA-Ames visualization group for having prepared Fig. 1. Thanks to M. Schüssler and M. Rempel for useful conversations. T.L.D. thanks the Stanford solar group for their hospitality. Observational data that are used in our analyses here are taken by the Helioseismic and Magnetic Imager and are publicly available at http://hmi.stanford.edu/. J. Leibacher and P.S. Cally are thanked for their careful reading of the manuscript and the considered comments that helped in improving it. We thank M. Miesch for sending us the simulation spectra.

1. Stein RF, Nordlund Å (2000) Realistic solar convection simulations. *Sol Phys* 192:91–108.
2. Vögler A, et al. (2005) Simulations of magneto-convection in the solar photosphere. Equations, methods, and results of the MURaM code. *Astron Astrophys* 429:335–351.
3. Rast MP (1998) Compressible plume dynamics and stability. *J Fluid Mech* 369:125–149.
4. Miesch MS (2005) Large-scale dynamics of the convection zone and tachocline. *Living Reviews in Solar Physics* 2:1–139.
5. Weiss A, Hillebrandt W, Thomas H, Ritter H (2004) *Cox and Giuli's Principles of Stellar Structure* (Princeton Publishing Associates, Cambridge, UK), Second edition.
6. Miesch MS, Brun AS, De Rosa ML, Toomre J (2008) Structure and evolution of giant cells in global models of solar convection. *Astrophys J* 673:557–575.
7. Ghizaru M, Charbonneau P, Smolarkiewicz PK (2010) Magnetic cycles in global large-eddy simulations of solar convection. *Astrophys J Lett* 715:L133–L137.
8. Käpylä PJ, Korpi MJ, Brandenburg A, Mitra D, Tavakol R (2010) Convective dynamos in spherical wedge geometry. *Astron Nachr* 331:73–81.
9. Käpylä PJ, Mantere MJ, Guerrero G, Brandenburg A, Chatterjee P (2011) Reynolds stress and heat flux in spherical shell convection. *Astron Astrophys* 531:A162–A180.
10. Hathaway DH, et al. (2000) The photospheric convection spectrum. *Sol Phys* 193:299–312.
11. Duvall TL, Jr, Jefferies SM, Harvey JW, Pomerantz MA (1993) Time-distance helioseismology. *Nature* 362:430–432.
12. Duvall TL, Jr (2003) *Nonaxisymmetric variations deep in the convection zone*, ed H Sawaya-Lacoste (ESA Special Publication), 517, pp 259–262.
13. Gizon L, Birch AC, Spruit HC (2010) Local helioseismology: three-dimensional imaging of the solar interior. *Annu Rev Astron Astr* 48:289–338.
14. Schou J, et al. (2011) Design and ground calibration of the Helioseismic and Magnetic Imager (HMI) instrument on the solar dynamics observatory. *Sol Phys* 274:229–259.
15. Hanasoge SM, Duvall TL, DeRosa ML (2010) Seismic constraints on interior solar convection. *Astrophys J Lett* 712:L98–L102.
16. Spruit HC (1974) A model of the solar convection zone. *Sol Phys* 34:277–290.
17. Gough DO (1977) Mixing-length theory for pulsating stars. *Astrophys J* 214:196–213.
18. Duvall TL, Jr, et al. (1997) Time-distance helioseismology with the MDI instrument: initial results. *Sol Phys* 170:63–73.
19. Gizon L, Birch AC (2004) Time-distance helioseismology: noise estimation. *Astrophys J* 614:472–489.
20. Marquering H, Dahlen FA, Nolet G (1999) Three-dimensional sensitivity kernels for finite-frequency traveltimes: the banana-doughnut paradox. *Geophys J Int* 137:805–815.
21. Duvall TL, Jr, Birch AC, Gizon L (2006) Direct measurement of travel-time kernels for helioseismology. *Astrophys J* 646:553–559.
22. Hanasoge SM, Duvall TL, Jr, Couvidat S (2007) Validation of helioseismology through forward modeling: realization noise subtraction and kernels. *Astrophys J* 664:1234–1243.
23. Nordlund Å, Stein RF, Asplund M (2009) Solar surface convection. *Living Reviews in Solar Physics* 6:1–116.
24. Trampedach R, Stein RF (2011) The mass mixing length in convective stellar envelopes. *Astrophys J* 731:1–7.
25. Spruit H (1997) Convection in stellar envelopes: a changing paradigm. *Memorie della Societa Astronomica Italiana* 68:397–413.
26. Kosovichev AG, et al. (1997) Structure and rotation of the solar interior: initial results from the MDI medium-L program. *Sol Phys* 170:43–61.
27. Kitchatinov LL, Ruediger G (1995) Differential rotation in solar-type stars: revisiting the Taylor-number puzzle. *Astron Astrophys* 299:446–452.
28. Balbus SA (2009) A simple model for solar isorotational contours. *Mon Not R Astron Soc* 395:2056–2064.
29. Rempel M (2005) Solar differential rotation and meridional flow: the role of a subadiabatic tachocline for the Taylor-Proudman balance. *Astrophys J* 622:1320–1332.

SUPPLEMENTARY MATERIAL: ANOMALOUSLY WEAK SOLAR CONVECTION

Shravan M. Hanasoge,[1,2], Thomas L. Duvall, Jr.,[3] & Katepalli R. Sreenivasan[4]

hanasoge@princeton.edu

Let us define the forward and inverse spherical-harmonic transforms thus

$$h_{\ell m} = \int_0^{2\pi} d\phi \int_0^{\pi} d\theta \ \sin\theta \ Y^*_{\ell m}(\theta,\phi) \ h(\theta,\phi), \tag{1}$$

$$h(\theta,\phi) = \sum_{\ell=0}^{L} \sum_{m=-\ell}^{\ell} h_{\ell m} \ Y_{\ell m}(\theta,\phi), \tag{2}$$

where (θ,ϕ) are co-latitude and longitude on the sphere, $Y_{\ell m}$ are spherical harmonics, ℓ the degree and m order.

Suppose we are interested in imaging a component p (longitudinal say) of sub-surface flows. Then we measure differential travel times $\delta\tau^p(\theta,\phi)$ (Duvall et al. 1993; Hanasoge et al. 2010) that are specifically sensitive to this component. For flows whose magnitude is much smaller than the local sound speed, travel times $\delta\tau^p(\theta,\phi)$ are assumed to be linearly related to the underlying flow field through the following left convolution relation (Driscoll & Healy 1994),

$$\delta\tau^p(\mathbf{\Omega}) = \int_\odot r^2 dr \int d\mathcal{R} \ \mathbf{K}^p(\mathcal{R}^{-1}\mathbf{\Omega}; r) \cdot \mathbf{v}(\mathcal{R}; r), \tag{3}$$

where $\mathcal{R}, \mathbf{\Omega}$ are elements in the Euclidean rotation group $SO(3)$, and we map functions from $SO(3)$ to S^2, the spherical surface. We denote the velocity field by $\mathbf{v}$, and the kernel by $\mathbf{K}^p$, r is radius, superscript p refers to component p of the flow (i.e., longitudinal, latitudinal or radial) that we are attempting to image. Ideally, the measurement we make will only be sensitive to the desired flow component p but since other flow components may also affect the measurement (i.e., leakage), it therefore is more generally sensitive to the full vector flow field. Because we are studying the problem in terms of spherical convolutions, we effectively assume that sensitivity kernels are laterally invariant.

First, we note that if we were to choose (for example)

$$\mathbf{v}(\theta,\phi,r) = v_0 \ \frac{\delta(r-r_0)\,\delta(\theta-\theta_0)\,\delta(\phi-\phi_0)}{\sin\theta_0} \ \mathbf{e}_p, \tag{4}$$

where v_0 is the amplitude of the delta function, then equation (3) becomes

$$\delta\tau^p(\theta,\phi) = v_0 \ \mathbf{K}^p(\mathcal{R}^{-1}(\theta_0,\phi_0); r_0) \cdot \mathbf{e}_p, \tag{5}$$

[1]Department of Geosciences, Princeton University, NJ 08544, USA

[2]Max-Planck-Institut für Sonnensystemforschung, 37191 Katlenburg-Lindau, Germany

[3]Solar Physics Laboratory, NASA/Goddard Space Flight Center, MD 20771, USA

[4]Courant Institute of Mathematical Sciences, New York University, NY 10012, USA

i.e., the travel-time map is a rotated version (by an amount (θ_0, ϕ_0)) of the kernel itself (Duvall et al. 2006; Hanasoge et al. 2007) at radial location $r = r_0$ and where we define the delta function as

$$\int_\odot r^2 dr\, \delta(r) = 1. \tag{6}$$

In order to mimic wave excitation in the simulations as it is thought to occur in the Sun, we excite waves using a frequency band-limited stochastic driver (Hanasoge et al. 2006), implying that there is realization noise associated with measurements of travel times from a finite-length temporal calculation. To improve the signal-to-noise ratio of the retrieved travel times, we introduce 500 randomly distributed delta flows, compute the travel-time map and rotate the local map around each map and average them together to obtain the sensitivity kernel.

The travel-time map in equation (3) is defined by three Euler angles. Consequently, a bijective mapping from $SO(3)$ to S^2 is possible only when we consider a suitable subset of rotations. An example is when $\mathbf{K}$ is azimuthally symmetric (such as a Gaussian), a situation in which one of the rotations is rendered redundant. While $\mathbf{K}$ is not axisymmetric, we find, to first order, that the azimuthally symmetric ($m = 0$) component of the kernel is a dominant contributor, a conclusion that is further supported by the nearly linear curve the regression analysis (e.g., Figure 1) produces. Assuming that the kernel may be written as such, we invoke the convolution theorem (Driscoll & Healy 1994), which tells us that the convolution (3) of such a function in spherical harmonic space may be written as,

$$\delta\tau^p_{\ell m} = \int_\odot r^2 dr\ \mathbf{K}^p_{\ell 0}(r)\ \cdot \mathbf{v}_{\ell m}(r). \tag{7}$$

In order to compute the kernel $\mathbf{K}^p_{\ell 0} \equiv \mathbf{K}^p_\ell$, we transform the travel times and delta-function-populated velocity field into spherical-harmonic space (also see appendix) and compute a linear regression between the two attendant sets of spherical harmonic coefficients at each ℓ (e.g., see Figures 1 and 2). In a previous work (Hanasoge et al. 2010), we computed the sensitivity of the measurement used here to flows taken from a snapshot of ASH simulations. The ASH layer is radially coherent over a much broader depth range than the delta-flows used in the current calibration (effective radial width of 4.1 Mm). Empirically we find an approximate linear relationship between the measured response and assumed thickness of the convective layer (see Figure 3).

The vector function $\mathbf{K}^p_\ell = [K^{pi}_\ell]$ is the sensitivity of the measurement aimed at imaging the p flow component of the underlying vector velocity field $\mathbf{v}_{\ell m} = [v^i_{\ell m}(r)]$. For example, if we were attempting to measure longitudinal flows, there may be leakage into the measurement from other flow components (latitudinal or radial).

Now we consider the variance of the travel times, averaged over many ensembles (denoted by angular brackets)

$$\langle \delta\tau^p_{\ell m} \delta\tau^p_{\ell m} \rangle = \sum_{i,j} \int_\odot r^2 dr \int_\odot r'^2 dr'\ K^{pi}_\ell(r)\ K^{pj}_\ell(r')\ \langle v^i_{\ell m}(r)\ v^j_{\ell m}(r') \rangle. \tag{8}$$

We assume that flow velocities at two different depths are independent of each other, thereby allowing us to write

$$\langle v^i_{\ell m}(r)\ v^j_{\ell m}(r') \rangle = \langle v^i_{\ell m}(r)\, v^j_{\ell m}(r) \rangle\ \delta(r - r'). \tag{9}$$

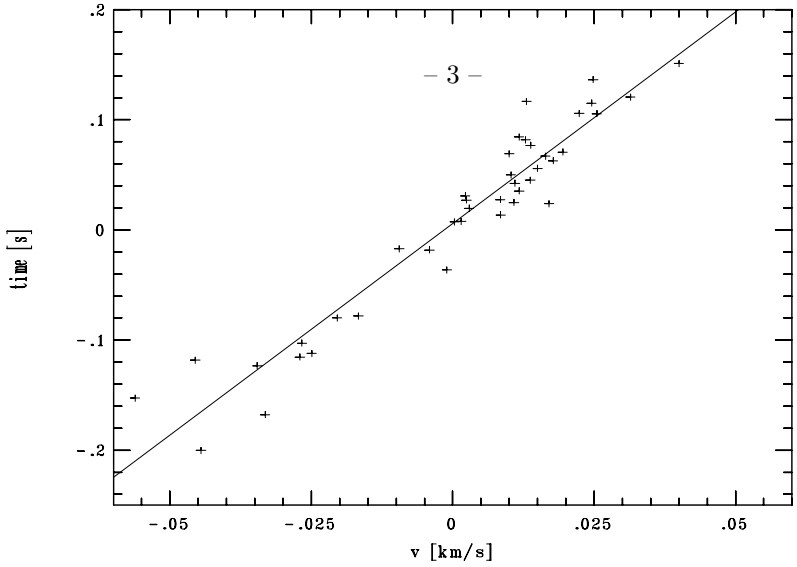

Fig. 1.— Linear regression analysis; spherical harmonic coefficients at $\ell = 20$, $m \in [-20, 20]$ of the longitudinal velocity component $v_{20,m}$ on the x axis and $\delta\tau^{\phi}_{20,m}$ on the y axis. The strong linear correlation between the two sets of coefficients, a relation that holds for all the coefficients, supports equation (7). The flows are tightly radially localized around $r/R_{\odot} = 0.96$.

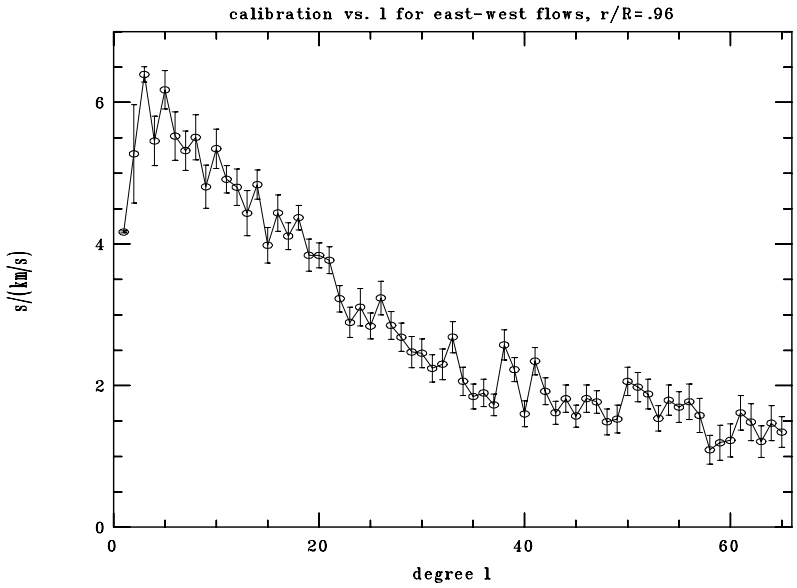

Fig. 2.— At each degree ℓ, we perform a regression analysis akin to the one described in the caption to Figure 1 and derive one calibration constant. Here we plot this calibration constant as a function of spherical-harmonic degree ℓ. It effectively describes the sensitivity of the measurement to longitudinal flows at $r/R_{\odot} = 0.96$ as a function of spatial scale of the flow. The error bars are at a 1-σ level (due to realization noise - introduced in the simulations in order to mimic the solar wavefield) - sensitivity is highest at the lowest degrees and drops with increasing wavenumber. The finite wave sensitivity up to $\ell \sim 65$ is indicative of a full spectrum of flows (i.e., delta-populated flows) that extends to high degrees in ℓ.

The variance now may be written as

$$\begin{aligned}\langle \delta\tau^p_{\ell m}\delta\tau^p_{\ell m}\rangle &= \int_\odot r^2dr\ K^{pp}_\ell(r)\,K^{pp}_\ell(r)\ \langle v^p_{\ell m}(r)\,v^p_{\ell m}(r)\rangle \\ &+ \sum_{i,j}^{i\neq p, j\neq p}\int_\odot r^2dr\ K^{pi}_\ell(r)\,K^{pj}_\ell(r)\ \langle v^i_{\ell m}(r)\,v^j_{\ell m}(r)\rangle, \end{aligned} \tag{10}$$

where the integral is split into two contributions, one due to the correlation between diagonal components of the kernels (the first term) and the other due to off-diagonal *leakage* between other components onto the desired measurement. Let us consider the case with $p = \phi$ (for argument's sake). Then, expanding equation (10) into its component terms, we have

$$\begin{aligned}\langle [\delta\tau^\phi_{\ell m}]^2\rangle &= \int_\odot r^2dr\Big\{[K^{\phi\phi}_\ell]^2\,\langle[v^\phi_{\ell m}]^2\rangle + [K^{\phi\theta}_\ell]^2\ \langle[v^\theta_{\ell m}]^2\rangle + [K^{\phi r}_\ell]^2\ \langle[v^r_{\ell m}]^2\rangle \\ &+ 2K^{\phi\theta}_\ell\,K^{\phi r}_\ell\ \langle v^r_{\ell m}\,v^\theta_{\ell m}\rangle + 2K^{\phi\theta}_\ell\,K^{\phi\phi}_\ell\ \langle v^r_{\ell m}\,v^\phi_{\ell m}\rangle + 2K^{\phi\phi}_\ell\,K^{\phi r}_\ell\ \langle v^\phi_{\ell m}\,v^\theta_{\ell m}\rangle\Big\}. \end{aligned} \tag{11}$$

The first three terms on the right side are positive definite, and we find that (using data shown in Figure 4)

$$K^{\phi\theta}_\ell\,K^{\phi r}_\ell,\ K^{\phi\phi}_\ell\,K^{\phi r}_\ell,\ K^{\phi\phi}_\ell\,K^{\phi\theta}_\ell \ll [K^{\phi\phi}_\ell]^2. \tag{12}$$

Assuming that the cross-component Reynold's stresses are comparable in magnitude to the kinetic energy terms, we have

$$\begin{aligned}\langle [\delta\tau^\phi_{\ell m}]^2\rangle &\approx \int_\odot r^2dr\ [K^{\phi\phi}_\ell]^2\,\langle[v^\phi_{\ell m}]^2\rangle + \int_\odot r^2dr\ [K^{\phi\theta}_\ell]^2\ \langle[v^\theta_{\ell m}]^2\rangle + \int_\odot r^2dr\ [K^{\phi r}_\ell]^2\ \langle[v^r_{\ell m}]^2\rangle, \\ \langle [\delta\tau^\phi_{\ell m}]^2\rangle &> \int_\odot r^2dr\ [K^{\phi\phi}_\ell]^2\,\langle[v^\phi_{\ell m}]^2\rangle. \end{aligned} \tag{13}$$

This argument holds for both lateral components, and we may write

$$\langle \delta\tau_{\ell m}\delta\tau_{\ell m}\rangle > \int_\odot r^2dr\ K_\ell(r)\,K_\ell(r)\ \langle v_{\ell m}(r)\,v_{\ell m}(r)\rangle, \tag{14}$$

where we have dropped explicitly stating p and velocity components are written as scalars. Since this term is positive definite, we may weaken the inequality further and apply integration limits around a specific depth range D (say around $r/R_\odot = 0.96$)

$$\langle \delta\tau^2_{\ell m}\rangle > \int_D r^2dr\ K^2_\ell(r)\ \langle v^2_{\ell m}(r)\rangle, \tag{15}$$

We assume that the kernel is a separable function, i.e., $K^2_\ell(r) = \mathcal{C}_\ell f(r)$, which is reasonable, since at depth, the kernel is radially localized and its horizontal structure is weakly dependent on depth. The term $\mathcal{C}_\ell$ is the calibration function that is obtained through the feature analysis. Defining

$$\zeta_{\ell m} = \int_D r^2dr\ f(r)\ \langle v^2_{\ell m}(r)\rangle, \tag{16}$$

where $\zeta_{\ell m}$ is the upper bound on the convective-velocity spectrum. We arrive at the desired inequality

$$\zeta_{\ell m} < \frac{\langle \delta\tau^2_{\ell m}\rangle}{\mathcal{C}_\ell}. \tag{17}$$

We show typical daily travel-time maps in Figure 5 and a synoptic solar rotation's worth of daily maps in Figure 6.

A. Details of the Method

Since we use numerical methods (Hanasoge et al. 2006) to simulate wave propagation, we must use finite-sized "delta" functions. Consider the problem of imaging the convection zone in the region $r/R_\odot \in [0.75, 1.0]$. Now, to compute the kernels and calibration curves to invert a given measurement to obtain the upper-bound flow spectrum, we need to determine the travel-time response to a delta flow at a series of depths. An individual "delta" function is defined as:

$$v_\phi^{(\delta)} = a \exp\left(-\frac{r^2 \sin^2\theta \Delta\phi^2 + r^2 \Delta\theta^2}{2\sigma_l^2} - \frac{\Delta r^2}{2\sigma_r^2} \right), \tag{A1}$$

Also, $\Delta\phi = \phi - \phi_c$, $\Delta\theta = \theta - \theta_c$, $\Delta r = r - r_c$, where (r_c, θ_c, ϕ_c) is the "location" of the anomaly and σ_r, σ_l are the radial and lateral widths of the flow deltas. We choose $\sigma_l = 3\sigma_r$ in our calculations.

- The first set of flows sits between 0.9932 and 0.9999, $r_c = 0.9966, \sigma_r = 1.62$,
- The second sits between 0.9760 and 0.9932, $r_c = 0.9846, \sigma_r = 1.62$ Mm,
- The third sits between 0.9455 and 0.9760, $r_c = 0.9607, \sigma_r = 1.74$ Mm,
- The fourth sits between 0.8995 and 0.9455, $r_c = 0.9205, \sigma_r = 2.96$ Mm,
- The fifth sits between 0.8364 and 0.8995, $r_c = 0.8659, \sigma_r = 2.96$ Mm,
- The sixth sits between 0.75 and 0.8364, $r_c = 0.7932, \sigma_r = 2.96$ Mm.

The choice of the radial and lateral widths of these features determines the calibration curve. The radial thickness of these features was varied in our experiment and we find an approximately linear relation between thickness and measured sensitivity (at least for the cases we considered).

500 longitudinal (in one set of simulations) and radial (in a different set of simulations) flow deltas were randomly distributed at a given radial location. Each delta flow was also randomly assigned a sign and thus with this large sample of flow deltas, the net or total flow is nearly zero. The amplitude was chosen to be 5% of the sound speed at r_c, i.e., $a = 0.05\ c(r_c)$.

The six data cubes listed above were generated. Then, to obtain the full 3D sensitivity kernel for each measurement geometry, the feature analysis was repeated on all six data cubes, giving us the sensitivity kernel at the depths listed above. So not only did we retrieve a calibration curve, but also extracted the full sensitivity kernels for all relevant measurement geometries.

REFERENCES

Driscoll, J. R., & Healy, D. M. 1994, Advances in Applied Mathematics, 15, 202

Duvall, Jr., T. L., Birch, A. C., & Gizon, L. 2006, ApJ, 646, 553

Duvall, Jr., T. L., Jefferies, S. M., Harvey, J. W., & Pomerantz, M. A. 1993, Nature, 362, 430

Hanasoge, S. M., Duvall, T. L., & DeRosa, M. L. 2010, ApJ, 712, L98

Hanasoge, S. M., Duvall, Jr., T. L., & Couvidat, S. 2007, ApJ, 664, 1234

Hanasoge, S. M., Larsen, R. M., Duvall, Jr., T. L., DeRosa, M. L., Hurlburt, N. E., Schou, J., Roth, M., Christensen-Dalsgaard, J., & Lele, S. K. 2006, ApJ, 648, 1268

Schou, J., Scherrer, P. H., Bush, R. I., Wachter, R., Couvidat, S., & Rabello-Soares, M. C. e. a. 2011, Solar Physics, Submitted

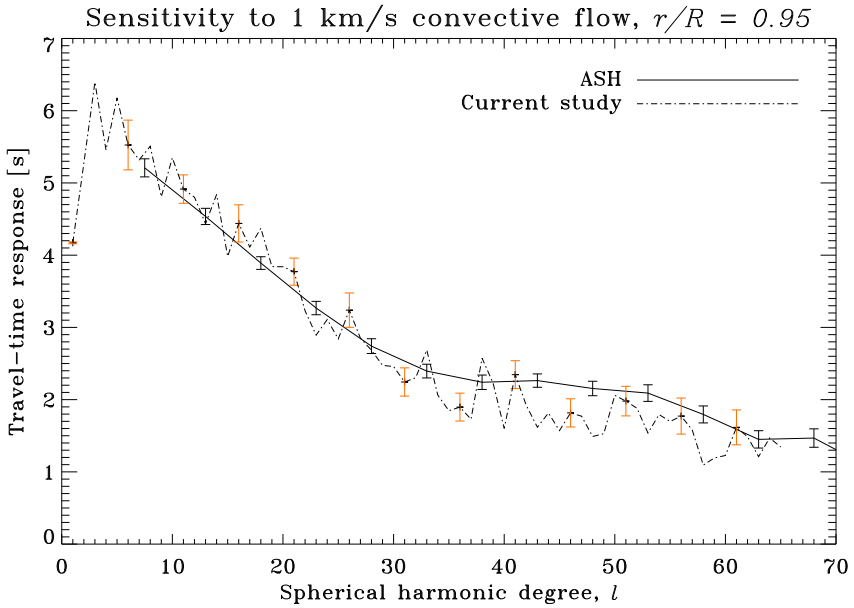

Fig. 3.— Normalized measurement sensitivities of waves to a flows from an ASH simulation (Hanasoge et al. 2010) with a focus depth of $r/R_\odot = 0.95$ and from the current study (red error bars; focus depth of $r/R_\odot = 0.96$). The ASH convective layer is radially much thicker than the delta-flows (4.1 Mm) used in the current calibration. We employ a simple normalization factor and divide the ASH sensitivity curve (Hanasoge et al. 2010) by the factor $22/4.1 = 5.4$. For the range considered here, we empirically find an approximate linear relationship between the response and assumed convective layer thickness.

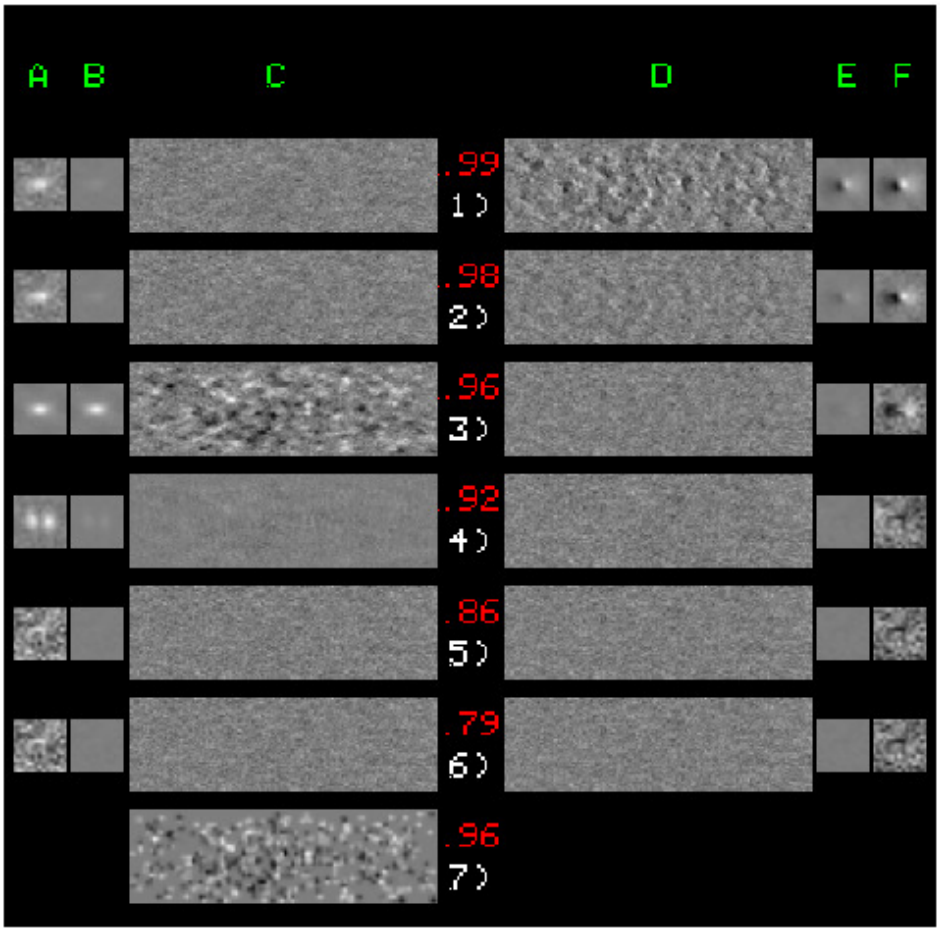

Fig. 4.— East-west travel time differences measured at the surface from simulations. Delta-function flows were introduced at various depths (denoted by r/R in red) and in the longitudinal and radial components. The time-distance geometry ('antenna') used has a focus depth of $r/R_\odot = 0.96$ and is primarily sensitive to east-west flows. All maps in columns C and D cover a longitude range of 330 degrees and latitude range of 101 degrees about the equator. Image 7C shows the input v_ϕ at $r/R = 0.96$ displayed in the range $\pm 3.5\,\mathrm{km\,s^{-1}}$. There are 500 randomly placed small features in this image, each with the same amplitude and randomly picked signs. C1 - C6 are maps of travel-time shifts induced by longitudinal delta-flows introduced at specific depths. D1-D6 represent the same but with radial delta-flows at those depths. Columns C and D, lines 1-6 are displayed in the range $\pm 15\,\mathrm{s}$. C1-6 describe the sensitivity of the measurement designed specifically to isolate longitudinal flows to such flows whereas D1-6 denote the undesired sensitivity to radial flow. In line with expectation, the largest responses are for signals that we are trying to extract, namely longitudinal flows at $r/R = 0.96$. To improve the signal to noise ratio, we average the local travel-time response about each of the (known) locations of the 500 individual features with the (known) signs taken into account. This improves the signal-to-noise ratio by a factor of $\sqrt{500} = 22$. In column B(E) is shown the spatial averages about the 500 features for column C(D) with the scale $\pm 5.4\,\mathrm{s}$. Column A(F) shows the images of column B(E) scaled to a value appropriate to each image. For A1-A6, the ranges are $\pm 0.7, \pm 0.7, \pm 5.4, \pm 5.4, \pm 0.7, \pm 0.7$ and for F1-F6, the ranges are $\pm 3.5, \pm 1.3, \pm 0.5, \pm 0.4, \pm 0.3, \pm 0.3$. The double feature in A4 presumably has to do with the opposite quadrants in the 'antenna'. The relatively strong response in D1 is caused by the rays being nearly vertical near the surface and the sensitivity to vertical flows there.

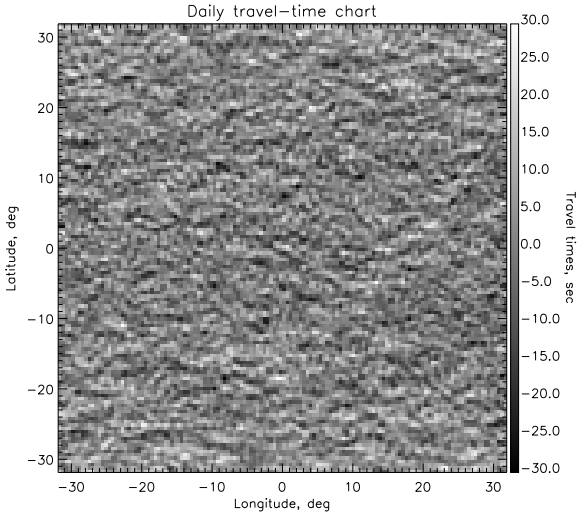

Fig. 5.— A travel-time map obtained by analyzing one day's worth of data taken by the Helioseismic and Magnetic Imager instrument (Schou et al. 2011) onboard the Solar Dynamics Observatory satellite. The spectrum of these travel times shows no significant peaks which meet the detection criteria.

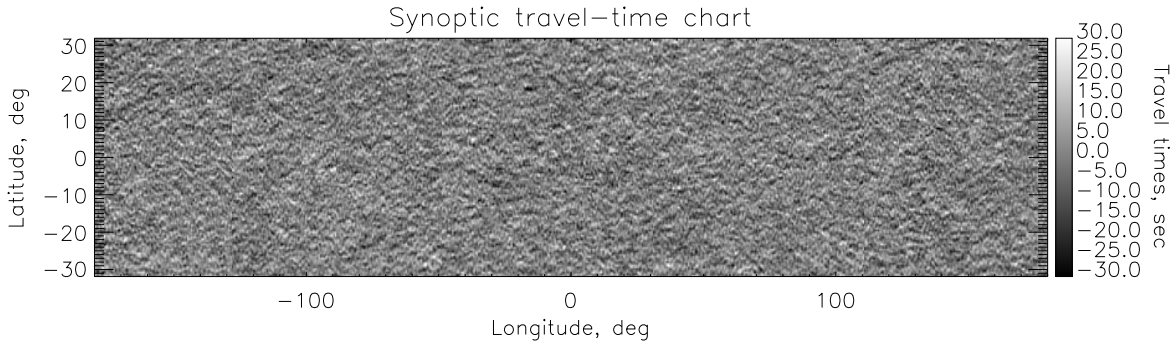

Fig. 6.— A synoptic travel-time chart formed by extracting and sticking together 13.2° each from a solar rotation's worth of daily maps (i.e., Figure 5). Like for Figure 5, the spectrum of these travel times shows no significant peaks which meet the detection criteria.